Stretching in Phase Space and Applications in General Nonautonomous Multi-Body Problems[*]

Cody R. Short · Daniel Blazevski
Kathleen C. Howell · George Haller

Abstract In the Circular Restricted Three-Body Problem (CRP), periodic orbits, stable and unstable manifolds, chaotic regions, and other dynamical features have all proven useful for engineering applications. These phase-space structures can be identified because the system is autonomous in a rotating frame. In more complex multi-body and high-fidelity models, classic invariant sets are not readily identifiable and new approaches are required. The approach here exploits the anisotropy of the growth or decay of perturbations to the trajectories, building on recent ideas from the theory of hyperbolic Lagrangian Coherent Structures (LCS). The present framework yields a mechanism to construct transfers in multi-body systems. In particular, it is applied to a restricted four-body problem and transfers are constructed requiring smaller Δv values than are necessary to accomplish the corresponding shift in Jacobi constant values for the associated embedded three-body problems.

Keywords Multi-body dynamical systems · Spacecraft trajectory design Cauchy–Green strain tensor · Finite-time Lyapunov exponent · Lagrangian coherent structures · Flow control segments

1 Introduction

Of fundamental importance in aerospace engineering, particularly within the field of astrodynamics, is a geometrical understanding of the possible motions a spacecraft or a satellite can assume under the influence of gravitational forces. In the

C. R. Short · K. C. Howell
School of Aeronautics and Astronautics, Purdue University, 701 West Stadium Avenue,
West Lafayette, IN 47907-2045, USA
E-mail: crshort@purdue.edu

D. Blazevski · G. Haller
Institute for Mechanical Systems, Department of Mechanical and Process Engineering,
ETH Zurich, Leonhardstrasse 21, Zürich, Switzerland

presence of one body, the Keplerian motion of the massless body is integrable and yields explicit analytical solutions. In the case of the Circular Restricted Three-Body Problem (CRP, or simply "restricted problem" throughout), the equations of motion are autonomous in a rotating frame, revealing periodic orbits, invariant manifolds, chaotic regions, and other classic phase-space structures. In more intricate gravitational fields, however, classical dynamical systems approaches do not apply. The goal of this work is to introduce new geometric techniques for such complex models.

A common technique for investigation in the restricted problem is leveraging the conservation of the Jacobi constant to generate a Poincaré section on a two-dimensional subsurface Σ. In more complex gravitational models, new strategies are required since (1) the trajectory may never return to Σ due to the lack of a conserved quantity, and (2) if, by chance, a trajectory does return to Σ at a point p, the map still depends on the initial time at which the trajectories are launched. Iterations may no longer be relevant: if $F_{t_o}(p)$ denotes the first return to Σ of a point p, then $F_{t_o}(F_{t_o}(p))$ has no physical meaning if the system is not autonomous in the given frame. The gravitational forces at time t_o differ from those at the time of the first return to $F_{t_o}(p)$.

Previous efforts to geometrically describe different trajectory behaviors employ the Finite-Time Lyapunov Exponent (FTLE) scalar field (Gawlik et al. 2009; Short et al. 2011; Pérez et al. 2012; Short and Howell 2014), which measures the locally largest stretching in the flow. The direction of largest stretching is also considered in this paper. These directions are exploited to identify useful paths of motion from an initial point and to parameterize regions that separate distinct trajectory patterns using the related notions of *stretchlines* associated with the largest stretching direction as well as reduced *strainlines*, respectively. These extensions are motivated by the recent notions of hyperbolic Lagrangian Coherent Structures (LCS) developed in Haller (2011), Farazmand and Haller (2012), and Blazevski and Haller (2014).

One advantage of the new concepts focused on stretchlines is the development of a mechanism to build low-energy transfer trajectories directly in many-body systems and models incorporating any degree of fidelity. This notion is illustrated through the construction of transfers from Oberon to Titania in a bicircular four-body model. Transfers are identified with Δv values smaller than those necessary to supply the theoretical energy change between the initial and final Jacobi constant values. In the process, the approach established here also clarifies the underlying dynamical structures.

The problem formulation and implementation of the methodology are described in detail throughout this document. In Section 2, related work is highlighted and the notion of LCS, as well as some underlying mathematical concepts, are discussed. Subsequently, in Sections 3–4, details of particular multi-body formulations and mapping strategies are summarized. Some background material follows directly from Short, Howell, and Tricoche (2011) as well as Short and Howell (2014). Given an initial point with a known maneuver to transport to a target, exploration of the nearby phase space using Flow Control Segments (FCS) to shorten transfer arc durations or reduce maneuver costs is considered in Section 5.1. Specifically, application of FCS and a targeting strategy, introduced by Schroer and Ott (1997) and further explored by Grebow (2010), are compared. A more generic example using FCS is also useful. The principal result from this analysis, featured

in Section 5.2, is a system-to-system transfer between two Uranian moons that illustrates the extension of FCS to more complex, nonautonomous systems.

2 Stretching in the linear flow

2.1 Singular stretching directions and values

Techniques using dynamical systems theory to investigate behavior in the CRP inherently rely on the iteration of a single map to assess the long-term dynamics, typically a Poincaré map on a two-dimensional surface Σ. In more complex gravitational fields, there is generally no low-dimensional map for which iterations can easily reflect the evolution of trajectories in the system. As an example, in the restricted problem, a fixed point p of the Poincaré map is a periodic orbit, yet for more complicated gravitational fields, points that satisfy $\phi_{t_\mathrm{o}}^{t_\mathrm{o}+T}(p) = p$ generally will not represent a periodic orbit unless the gravitational field itself is periodic. Even if the gravitational field is periodic in time in a certain frame, techniques to search for periodic orbits and invariant manifolds are limited.

In the current analysis a fixed interval of time, T, is considered and the flow map, $\phi_{t_\mathrm{o}}^{t_\mathrm{o}+T}$, is evolved over $[t_\mathrm{o}, t_\mathrm{o} + T]$ without iterating the map. The linear flow from the State Transition Matrix (STM), $D\phi_{t_\mathrm{o}}^{t_\mathrm{o}+T}$, yields a first-order approximation to trajectories near a reference path. Perturbations can exhibit dramatically distinct patterns of divergence, compression or lack of either. The characterization of such behavior is encoded in the *singular values* σ_i and the unit length *singular vectors* $\boldsymbol{\xi}_i$ and $\boldsymbol{\theta}_i$ of $D\phi_{t_\mathrm{o}}^{t_\mathrm{o}+T}$ satisfying,

$$D\phi_{t_\mathrm{o}}^{t_\mathrm{o}+T}\boldsymbol{\xi}_i = \sigma_i\boldsymbol{\theta}_i. \tag{1}$$

The term *singular* reflects that σ_i are stationary values of the function,

$$\sigma = \frac{\left|D\phi_{t_\mathrm{o}}^{t_\mathrm{o}+T}\boldsymbol{\xi}\right|}{|\boldsymbol{\xi}|}, \tag{2}$$

with respect to changes in the direction $\boldsymbol{\xi}$. The singular vectors $\boldsymbol{\xi}_i$ are also eigenvectors of the Cauchy–Green Strain Tensor (CGST), $\mathbf{C}_{t_\mathrm{o}}^{t_\mathrm{o}+T} = \left(D\phi_{t_\mathrm{o}}^{t_\mathrm{o}+T}\right)^{\mathsf{T}} D\phi_{t_\mathrm{o}}^{t_\mathrm{o}+T}$ (Smith 1993), and the corresponding eigenvalues of $\mathbf{C}_{t_\mathrm{o}}^{t_\mathrm{o}+T}$ are $\lambda_i = \sigma_i^2$ (the notation $^\mathsf{T}$ indicates the matrix transpose). The largest singular value σ_n corresponds to the largest possible growth of a perturbation, with the growth exponent

$$\mathrm{FTLE} = \frac{1}{|T|}\log\sigma_n = \frac{1}{|T|}\log\sqrt{\lambda_n} \tag{3}$$

defined as the finite-time Lyapunov exponent. The eigenvalues and eigenvectors of $\mathbf{C}_{t_\mathrm{o}}^{t_\mathrm{o}+T}$ are computed to implement the strategies in the following analysis.

Both the FTLE and the eigenvectors of the CGST are related to the recent notion of Lagrangian Coherent Structures (LCS) in fluid dynamics. The LCS-based methodology developed here extends previous work by introducing the notions of Flow Control Segments (FCS; Section 2.2) and tensorlines in an astrodynamical context (Section 2.3). These concepts appear in a number of examples and supply

a framework for targeting and transfer problem analysis in nonautonomous multi-body systems. In previous investigations, Anderson, Lo, and Born (2003) discuss the application of FTLE over relatively short time spans, denoting the metric as the Local Lyapunov Exponent (LLE), to identify sensitive regions along a trajectory. Improved patch point placement for differential corrections strategies using FTLE values is investigated by Harden (2013) and Harden et al. (2014). Various authors, including Lara, Russell, and Villac (2007), Villac (2008), and Villac and Broschart (2009), all apply the Fast Lyapunov Indicator (FLI), a metric similar in form to FTLE, for preliminary spacecraft trajectory design and stability analyses in multi-body environments. Detection of the Arnold web in phase space using the FLI is offered by Froeschlé, Guzzo, and Lega (2001). In an application more closely associated with this investigation, Gawlik et al. (2009) examine LCS in the mixed position–velocity phase space of the planar elliptic restricted three-body problem. Additional efforts to apply FTLE and LCS methods in the three-body problem within the context of periapse mappings are offered by Short, Howell, and Tricoche (2011). Pérez, Gómez, and Masdemont (2012) also examine the detection of invariant manifolds from LCS in the circular restricted three-body problem. An examination of the impact of increasing the fidelity of the multi-body model on FTLE analysis and LCS-guided design is investigated by Short and Howell (2014). Identification of linked orbits in the four-body problem using LCS is considered by Oshima and Yanao (2014).

2.2 Flow control segments

The notion of control segments is introduced by Shinbrot, Ott, Grebogi, and Yorke (1990) with further extensions by Schroer and Ott (1997). In Schroer and Ott, the authors employ small lines or circles about specific points on a Poincaré map to join two periodic orbits from different regions in the chaotic CRP phase space. Working in the planar CRP, a map is defined in terms of position and velocity (Cartesian x and $\dot{x}$) states in the rotating frame. A strategy where a segment and circle are simultaneously iterated forward from the vicinity of an initial orbit and backward from a target orbit on the map is utilized. As the segments are advected under the flow, their pre- or post-images grow until, after some (likely different) number of forward and backward iterations, an intersection occurs. This process is illustrated in Figure 1, reproduced from Schroer and Ott (1997) with permission.

Such an intersection is a connection in all components of the planar CRP state and represents an end-to-end trajectory joining the orbits with small velocity discontinuities at departure and insertion. In Grebow (2010), the example from Schroer and Ott is revisited. Grebow observes that the natural stretching of the target circle quickly collapses it to an arc. Thus, the process is equally well served by employing segments for both forward and backward evolution.

In the present paper, similar *Flow Control Segments* (FCS) are constructed along the eigenvector, $\boldsymbol{\xi}_n$, associated with the largest eigenvalue of the Cauchy–Green tensor (these FCS are, in fact, applied stretchlines of the tensor). Assuming an appropriate time scale for calculating the CGST, stretching occurs in the phase space along the eigenvector, $\boldsymbol{\xi}_i$, proportional to $\sqrt{\lambda_i}$, that is,

$$\left| \mathrm{D}\phi_{t_\circ}^{t_\circ + T} \boldsymbol{\xi}_i \right| = \sqrt{\lambda_i} \left| \boldsymbol{\xi}_i \right|, \tag{4}$$
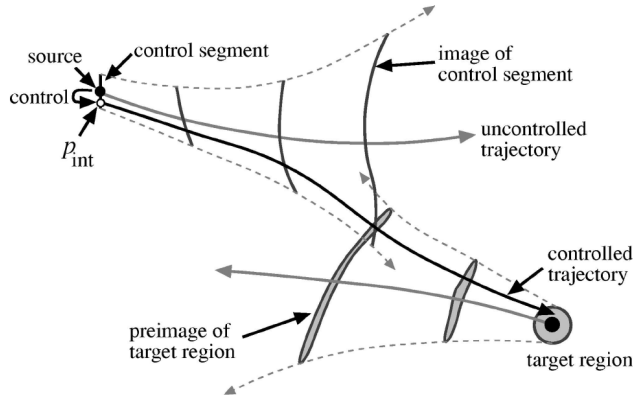
Fig. 1: Forward–Backward Method of Shinbrot et al. (1990) (Figure Reproduced from Schroer and Ott (1997) with Publisher's Permission)

thus, $\boldsymbol{\xi}_n$ supplies the most-stretching direction in the flow, and represents the optimal choice for divergent behavior. Consequently, the images resulting from evolving $\boldsymbol{\xi}_n$-aligned segments intersect after fewer iterations yielding a shorter time-duration transfer. This notion is illustrated in Figure 2, where the double-headed red arrow represents $\boldsymbol{\xi}_n$ and the double-headed blue arrow conveys the remaining directions.
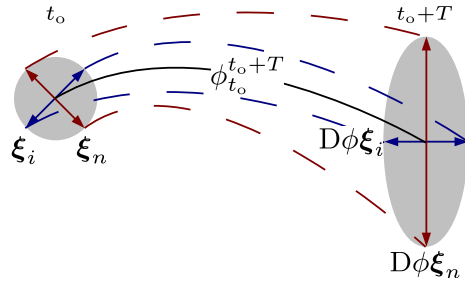
Fig. 2: Stretching Associated with Eigenvectors of the Cauchy–Green Tensor

2.3 Tensorlines of the Cauchy–Green strain tensor

Curves tangent to direction fields associated with $\mathbf{C}_{t_o}^{t_o+T}$ are tensorlines, and tensorlines that are tangent to the direction of largest stretching are termed *stretch-lines*. On the other hand, in two-dimensional flows, for example, curves tangent to $\boldsymbol{\xi}_1$ are orthogonal to the largest stretching direction $\boldsymbol{\xi}_2$ and maximally repel nearby trajectories at each point (Farazmand and Haller 2012)—these lines are repelling *strainlines*. A generalization to three-dimensional flows is given in

Blazevski and Haller (2014), where reduced repelling strainlines are computed on two-dimensional restrictions of the initial conditions. The reduced strainlines in Blazevski and Haller (2014) are obtained by seeking intersections of surfaces orthogonal to the most stretching direction $\boldsymbol{\xi}_3$ with a 2D set of initial conditions.

A further generalization of the reduced field approach of Blazevski and Haller (2014) is accomplished by similarly computing reduced strainlines on select 2D surfaces of initial conditions. More specifically, given a two-dimensional set of initial conditions Σ, let $\boldsymbol{n}_1$ and $\boldsymbol{n}_2$ be two linearly independent vectors orthogonal to Σ to produce a four-dimensional planar phase space. For any point p on Σ, the unique direction $\hat{\boldsymbol{\xi}}_4$, orthogonal to $\boldsymbol{n}_1$, $\boldsymbol{n}_2$ and $\boldsymbol{\xi}_4$, is the intersection of repelling Lagrangian coherent structures with the set Σ (Haller 2011). The approach in this work to compute intersections of three-dimensional surfaces orthogonal to $\boldsymbol{\xi}_4$, generalizes the method of Blazevski and Haller (2014) for computing analogous intersections in 3D flows. For the spatial restricted problem, four linearly independent directions normal to Σ are required and, then, the unique direction orthogonal to the four normal vectors and $\boldsymbol{\xi}_6$, $\hat{\boldsymbol{\xi}}_6$, can be constructed.

2.4 Computing the CGST, FTLE and strainlines

Since strainlines are curves tangent to a direction field obtained from the eigenvectors of CGST, an accurate computation of the tensor is necessary. In line with Farazmand and Haller (2012) as well as Blazevski and Haller (2014), the CGST is computed on a grid $\mathbf{X}_i$ of points using finite differencing. At each point, a uniform h is used for the finite difference approximation, and h need not be the distance between the grid cell $|\mathbf{X}_i - \mathbf{X}_j|$ (it is generally several orders of magnitude smaller for the examples in this paper). This approach is typically more accurate and numerically robust than computing the CGST by integrating the equations of variation. This additional numerical stability is a consequence of the fact that the grid approach reflects the actual fate of each perturbation, while the entries of the propagated STM can grow exponentially.

At each point $\mathbf{X}_i$, the FTLE is computed from $\mathbf{C}_{t_o}^{t_o+T}$ using Equation (3). Reduced strainlines are computed by integrating the reduced field $\hat{\boldsymbol{\xi}}_n$; however, the field is defined only up to a sign. An additional step is required to clarify the sign ambiguity. As for the two- and three-dimensional phase-space flows (Farazmand and Haller 2012; Blazevski and Haller 2014), the differential equation is solved for parameterizations $\mathbf{r}$ of reduced strainlines,

$$\frac{d}{ds}\mathbf{r}\left(s\right) = \operatorname{sign}\left(\left\langle \hat{\boldsymbol{\xi}}_n\left(\mathbf{r}\left(s-\varDelta\right)\right), \hat{\boldsymbol{\xi}}_n\left(\mathbf{r}\left(s\right)\right)\right\rangle\right) \hat{\boldsymbol{\xi}}_n\left(\mathbf{r}\left(s\right)\right). \tag{5}$$

Thus, to compute curves tangent to $\hat{\boldsymbol{\xi}}_n$, the previous orientation of $\hat{\boldsymbol{\xi}}_n$ is assessed to accommodate a sign change in $\hat{\boldsymbol{\xi}}_n$ at the next time step if appropriate.

3 System models

The computation of the CGST is not contingent on any assumptions in the derivation of the system differential equations and, thus, can be applied to systems

modeled with various levels of fidelity. Analysis based on the Cauchy–Green tensor remains valid regardless of the complexity of the model. Flow control segments are investigated in examples within the context of the circular restricted problem as well as a bicircular four-body system in this paper. Selected results are transitioned through various levels of fidelity and are ultimately validated in a partial ephemeris model. Some necessary considerations for each model are summarized.

3.1 The restricted three-body model

Some key space environments involve multiple gravity fields. Therefore, it is often necessary to incorporate as many of these gravity fields as possible into the governing models to ensure accurate simulation and to capture the essential features of the dynamical interactions.

The CRP is the simplest model for the motion of a massless object in the presence of two massive bodies. Though it offers no closed-form analytical solutions (Diacu 1996), it has been thoroughly studied numerically, and has been of significant practical importance in applications. For completeness, the definition and parameters of the CRP are recalled. The two primary bodies that appear in the model are designated as P_1 and P_2. Position variables, x, y, and z describe the position of the third body, the spacecraft, with respect to the barycenter of the primary system, which also serves as the origin of the rotating and inertial reference frames. The system mass parameter is represented by $\mu = \frac{m_2}{m_1 + m_2}$, a function of the masses of the primary bodies. Additionally, distances between the third body and each of the two primaries are denoted r_{i3}. In a coordinate frame that rotates coincident with the circular primary motion, a system of differential equations that describes the motion of the third body incorporates the potential function,

$$U^* = \frac{1-\mu}{r_{13}} + \frac{\mu}{r_{23}} + \frac{1}{2}(x^2 + y^2), \tag{6}$$

and is written,

$$\ddot{x} = \frac{\partial U^*}{\partial x} + 2\dot{y}, \quad \ddot{y} = \frac{\partial U^*}{\partial y} - 2\dot{x}, \quad \ddot{z} = \frac{\partial U^*}{\partial z}, \tag{7}$$

where the first derivatives in x and y appear as a result of the Coriolis acceleration.

The equations of motion in the restricted problem are consistent with Szebehely (1967) where they admit a single integral of the motion. This integral is termed the Jacobi integral and is represented as C in this analysis,

$$C = 2U^* - v^2, \tag{8}$$

where $v^2 = \dot{x}^2 + \dot{y}^2 + \dot{z}^2$, that is, the square of the magnitude of the relative velocity. This integral allows for a reduction of order in the problem, and frequently serves in an important role in the definition of maps. The Jacobi integral reveals boundaries on the motion of the third body in the restricted problem. These boundaries are defined when the velocity in Equation (8) is zero, separating regions of real and imaginary velocities. An example of the Jacobi limiting boundaries, or Zero Velocity Curves (ZVC) in the x–y plane (plotted in black), is depicted in Figure 3 along with the two libration points near the second primary (in this case, Saturn
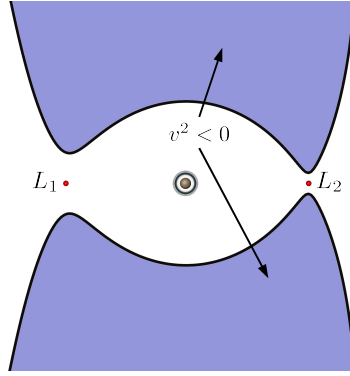
Fig. 3: Zero Velocity Curves in the P_2 Region

at $50\times$ scale in the Sun–Saturn system). These types of boundaries on the motion are intimately associated with the definitions of the maps employed here.

The restricted problem represents a model of sufficient complexity to exhibit regions of both chaotic and ordered behavior. Generally, the focus of the analysis in this model is understanding and exploiting any dynamical structures that are associated with the chaotic regions to identify useful trajectory arcs. The CRP model is frequently suitable to yield first-order mission design solutions, but useful information is often difficult to isolate amidst the chaos.

3.2 The bicircular four-body model

A simplified four-body model, similar to the model utilized by Koon, Lo, Marsden, and Ross (2002) and further explored by Blazevski and Ocampo (2012), is also employed here. This model incorporates the influence of a third massive body simultaneously with the dynamical effects of the two primary bodies in the circular restricted problem. For a particular planet-moon example, Uranus, Titania, Oberon and a spacecraft comprise the four-body system. A specific orientation of the relative geometry in such a system, e.g., in a Uranus–Titania rotating frame, appears in Figure 4. The orbital angle that defines the initial position of the fourth body, measured counter-clockwise with respect to the rotating x axis, is denoted $\theta_{\rm o}$ (in the example figure, $\theta_{\rm o} = \frac{\pi}{4}$ radians, or $45^{\rm o}$).

Under this model, all three massive primaries describe circular orbits about the barycenter of the first and second primaries (Uranus, Titania). The additional massive primary is designated P_4 (Oberon). Although the system is not coherent, the Newtonian inverse-square gravity of P_4 acts on the spacecraft in addition to the gravitational effects of the two CRP primaries. The third primary body does not affect the circular orbits of the other primaries. The equations of motion remain the same as Equations (7), but the potential function is now (Guzman 2001),

$$U^* = \frac{1 - \mu}{r_{13}} + \frac{\mu}{r_{23}} + \frac{\mu_4}{r_{43}} + \frac{1}{2}(x^2 + y^2), \qquad (9)$$

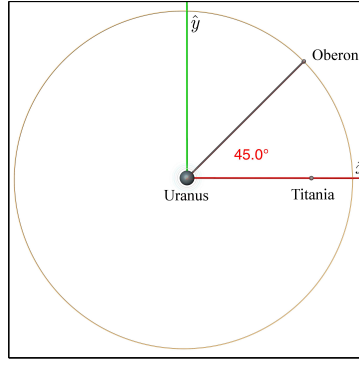where $\mu_4 = \frac{m_4}{m_1 + m_2}$.

Fig. 4: A Sample Configuration of the Bicircular Four-body Problem

The bicircular four-body model, while still incorporating significant simplifica-tions, introduces an important transition. The presence of the perturbing fourth body results in a nonautonomous system. The system is time-periodic and could be made autonomous through a temporal or stroboscopic mapping, though this mapping is at least four dimensional, nonintegrable and will typically not allow any conserved quantities to reduce the dimension of the system. Thus, classical techniques, e.g., locating fixed points of a two-dimensional Poincaré mapping, are rather limited. Periodic orbits reminiscent of Lyapunov orbits may exist in the full four-body example (e.g., Blazevski and Ocampo (2012)), but only isolated cases are apparent and there is not yet a systematic procedure to detect families of periodic orbits, if such a family exists. The goal of this analysis is to highlight the applicability of LCS notions to nonautonomous systems, and this work yields a understanding not obtainable through the use of any temporal stroboscopic mappings. The transition in the nature of the system decreases or eliminates the applicability of many of the dynamical systems tools that are available in the CRP. A constant of the motion, and, consequently, a convenient expression for bounds on the motion, is no longer available. Due to the time-dependent nature of the underlying flow, the focus now shifts to the initial system geometry.

3.3 Partial ephemeris model

A partial ephemeris model is selected to be generally consistent with the previ-ous models. This higher-fidelity model, similar to the model employed by Pavlak and Howell (2012), is constructed to validate the solution obtained from simpler models by incorporating position histories for the primary bodies supplied by JPL ephemeris solutions. The model is designated a "partial" ephemeris model because only the primary bodies of interest (as point masses), and no higher-order perturb-ing effects, are included. The governing equations are then derived as the n-body relative equations of motion,

$$\ddot{\boldsymbol{r}}_{qs} = -\frac{\mu_{2b,s} + \mu_{2b,q}}{r_{qs}^3}\boldsymbol{r}_{qs} + \sum_{\substack{j=1 \\ j \neq s,q}}^{n} \mu_{2b,j}\left(\frac{\boldsymbol{r}_{sj}}{r_{sj}^3} - \frac{\boldsymbol{r}_{qj}}{r_{qj}^3}\right). \tag{10}$$

Where μ_{2b} is the familiar mass parameter from the two-body problem, nondimensionalized as appropriate. The position vector, $\boldsymbol{r}_{qj}$, indicates the position of the jth body with respect to the central body, q; the subscript s is associated with the spacecraft. In this model, states defined in the restricted problem are transitioned to body-centered J2000 states via an instantaneous rotating frame defined by ephemerides.

This partial ephemeris model naturally involves six-dimensional state vectors and trajectory propagation proceeds in all spatial dimensions. Additionally, computation of the CGST employs "auxiliary grid" points about each state variable. Thus, in this model, one CGST computation involves the propagation of 12 perturbations. Notwithstanding these spatial considerations, since the maps are transitioned from the planar lower-fidelity model, their domain remains the same.

These models illustrate the wide applicability of LCS analysis to different types of systems. Ultimately, this extensibility indicates that this type of strategy can be employed for a full-ephemeris design and analysis. Such capability is supported by previous literature in other fields (Mathur et al. 2007; Peacock and Dabiri 2010), which describe the Cauchy–Green tensor as a tool for directly analyzing empirical flow results (when no underlying dynamical model is available).

4 Maps

Mapping analysis within the context of multi-body regimes has proven to effectively reveal design options that are otherwise difficult to identify (see, for example, Davis and Howell (2012)). Some advantages of a map-based approach include a broader view of the design space as well as a cleaner visual that offers easier categorization of the behavior in a specific region. The maps employed in this analysis generally employ relatively well-known mapping strategies. These maps offer a Lagrangian perspective and essentially reflect the fate of a grid of initial conditions in terms of their FTLE values associated with some propagation time.

4.1 State-space maps

Analysis in many systems involves a classical Poincaré mapping to create a puncture plot that facilitates the investigation. Such a map reveals salient information by reducing the dimension of the system. Under this Poincaré mapping approach, a hyperplane corresponding to some value of a single state variable is defined. A grid supplies the relationship between two other state variables, and the fourth state is constrained by a system integral (for a 4D phase space).

While there are many possible map representations available for observing the behavior in a system, strategies frequently involve the investigation of position–velocity phase spaces. For example, a map can be plotted in terms of a position variable and its associated velocity component. Maps in the y–$\dot{y}$ and x–$\dot{x}$ phase spaces are both used in this investigation, the former employed for FTLE maps and the latter for puncture plots.

4.2 Stroboscopic FTLE maps and associated strainlines

Traditional stroboscopic maps are constructed as Poincaré maps with a hyperplane condition selected as a particular time, for example, the characteristic period of

a system. The time should not be arbitrarily defined, however, if the desire is to iterate the map. Consider the map $F = \phi_{t_o}^{t_o+T}$; then, $F \circ F$, two iterations of F, has no physical meaning, unless the gravity field is periodic in the frame of integration. Alternatively, composing $F_1 = \phi_{t_o}^{t_o+T}$ and $F_2 = \phi_{t_o+T}^{t_o+2T}$ does have meaning since $F_1 \circ F_2$ is physically meaningful, i.e., $\phi_{t_o}^{t_o+2T}$. In this case, though, fixed points of F_1 generally have no meaning or interest beyond $t_o + T$.

Rather than searching for periodic orbits and manifolds in systems with complicated time-dependence, an alternate strategy of exploiting FTLE maps and associated strainlines is employed here. One essential value of the FTLE for predicting behavior is captured by examining large groupings of FTLE values in a region. This approach leads directly to creating maps of FTLE values. Aspects from the various types of mapping strategies can be combined to effectively illustrate the flow in an astrodynamical model. The information that emerges from these maps is then incorporated into different phases of mission design and analysis.

5 Applications

A few selected examples demonstrate potential strategies for utilizing insight from the largest stretching direction. Targeting, or control, segments are developed as a first example, both with and without the flow context provided from the CGST. This comparison is followed by a generalized example of the implementation of flow control segments. The main result of the paper highlights the extensions of these schemes to nonautonomous systems.

5.1 FCS targeting

The forward and backward time-advection of small segments bracketing a control point, denoted control segments, is investigated by Shinbrot et al. (1990), further expanded by Schroer and Ott (1997) and revisited by Grebow (2010). These control segments are created as small segments along a particular velocity component without consideration of the underlying flow behavior. This initialization approach is a consequence of the desire to vary velocity only in a "feasible" direction while restricting any variation in initial or final position to zero. However, small adjustments in the direction of the phase space that naturally leads toward greater flow divergence augments the approach of joining forward and backward segments, producing a trajectory that can subsequently be corrected with a differential corrections scheme. Thus, control segments constructed exploiting the flow context may yield a better result depending on the desired trajectory characteristics.

5.1.1 Comparing control segments with and without flow-based context.

Schroer and Ott produce an example to illustrate forward-time control segment advection and backward-time target region advection to join two periodic orbits in the Earth–Moon circular restricted three-body problem. In the following example, the mass-parameter and energy levels are consistent with Schroer and Ott ($\mu = 0.0123$, and $C = 3.17948$). The initial and final periodic orbits are generated numerically after observation of the trajectory characteristics as elaborated by

Grebow. The following orbits and the associated map representations compare
closely with Grebow. The initial orbit, in this case, is a period-3 orbit and is
depicted in green in Figure 5(a), along with the final orbit about the Moon (red).
The initial points on both orbits are marked with black arrows near the x axis; the
forward time evolution from both points is in the positive y direction. Moreover,
the trajectories are subsequently represented as fixed points (both numbered as
iteration "0" for their propagations) on the x–$\dot{x}$ phase-space Poincaré map in
Figure 5(b). From the control points on the map, small segments (magnitude
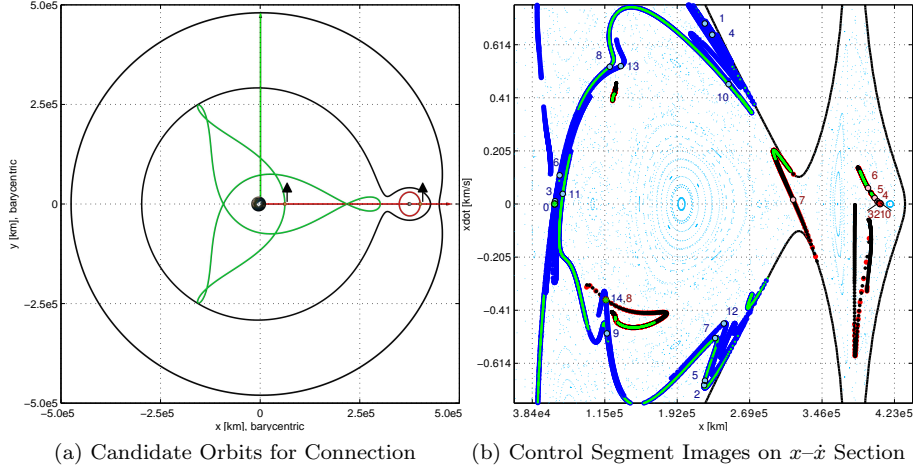1×10^{-4}) are created along the map-space components of the eigenvector associated

(a) Candidate Orbits for Connection   (b) Control Segment Images on x–$\dot{x}$ Section

Fig. 5: Orbits and Control Segments

with the largest eigenvalue of the Cauchy–Green tensor, that is, along $\boldsymbol{\xi}_2$, in this
case. These segments are, in fact, stretchlines that are used as control segments,
and are termed *Flow Control Segments* (FCS) given their incorporation of the flow
behavior. The CGST is computed only with respect to the map via finite-difference
derivatives in x and $\dot{x}$ for this case. The integration time for the Cauchy–Green
tensor is generally selected as appropriate for the time scale of the application.
For this example, it is observed that the time to reach the first crossing of the
map is sufficient to yield predictive CG eigenvectors. The control segments are
evolved under the flow of the system backward and forward in time from the
lunar-proximal control point and triply-periodic control point, respectively. For
comparison with the previous investigations of this specific example, segments
along only $\dot{x}$ as well as a segment defined as a circle about the control point
near the Moon are also integrated. The images of each of these curve evolutions
corresponding to iterations of the map also appear in Figure 5(b). The curves are
colored based on their initial nature: green curves result from advection of purely
$\dot{x}$ segments, red and blue curves from the $\boldsymbol{\xi}_2$-aligned FCS and, in the case of the
circular target region, black points mark the associated curves. Observation of
the initial backward iterations of the circular target region reveals that it quickly
deforms to align with the flow control segment, a fact that is exploited to verify the

CG integration time in this case—if the circular region deforms to conform with images of $\boldsymbol{\xi}_2$, the time scale is appropriate. Later iterations in both time directions reflect longer curves associated with the flow-aligned control segments; the green points resulting from the initial $\dot{x}$ segments require additional iterations before an intersection is observed. Also marked on Figure 5(b) are the map crossings associated with trajectory arcs that intersect after 14 forward iterations from a perturbation off the triply-periodic orbit and 8 backward iterations from the lunar orbit step-off.

The trajectory arcs necessarily include discontinuities at the departure and arrival points. Since perturbations are introduced along the eigendirection, these discontinuities are in position as well as velocity. Moreover, rather than employ an iterative scheme such as bisection to refine the intersection between the forward and backward arcs, a slight discontinuity is allowed at this point as well. These discontinuities are resolved by implementing a parallel shooting differential corrections scheme as described by Pavlak (2013). Upon convergence of the corrections process, the only remaining discontinuities are the requisite velocity changes to render the transfer. Figure 6 includes views of the backward arc and the differentially corrected CRP solution. The connection point is visible where the backward
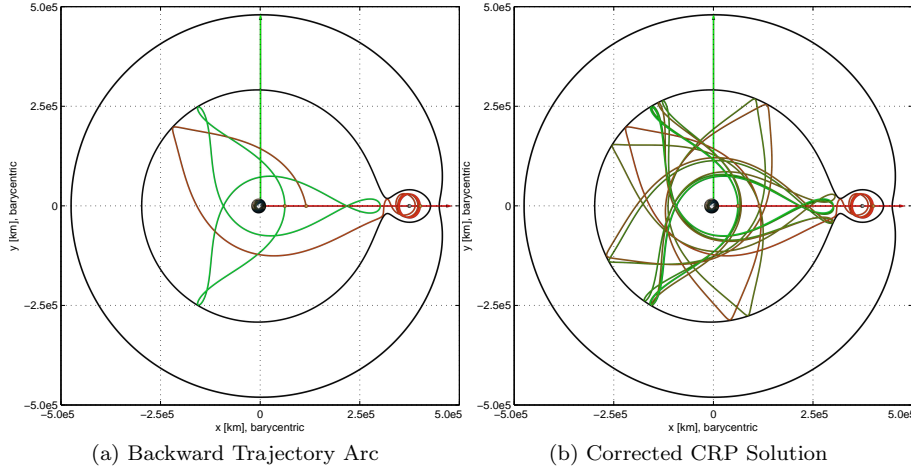

(a) Backward Trajectory Arc   (b) Corrected CRP Solution

Fig. 6: Connected Forward and Backward Segments

propagation meets the x axis ($x \approx 100{,}000$ km). The trajectory evolution in time is reflected in color by a gradual transition from green to red. The maneuver requirement at departure is 1.99 $\frac{m}{s}$, while the Δv upon arrival is 1.04 $\frac{m}{s}$ (total: 3.03 $\frac{m}{s}$). These maneuver costs compare with one of the examples from Schroer and Ott at 0.62 $\frac{m}{s}$ and 2.61 $\frac{m}{s}$, respectively, for a total of 3.23 $\frac{m}{s}$. They likewise compare with figures reported by Grebow for a somewhat qualitatively different solution—0.39 $\frac{m}{s}$ and 1.46 $\frac{m}{s}$ (total: 1.85 $\frac{m}{s}$). A significant difference, and potential advantage of the FCS approach, is a shorter time-of-flight. Each example reported in previous references requires more than 290 days; the sample transfer here is completed in 265 days. This shorter duration is a direct consequence of the FCS strategy with

a path that reaches an intersection in fewer iterations given maximal stretching from $\boldsymbol{\xi}_2$-aligned FCS.

The given solution can be validated in a more complete model. For a carefully selected initial epoch, the CRP solution is transitioned into the higher-fidelity ephemeris n-body model. In this case, only the ephemerides of the Earth and Moon are included. Views of the transitioned solution appear in Figure 7; the states
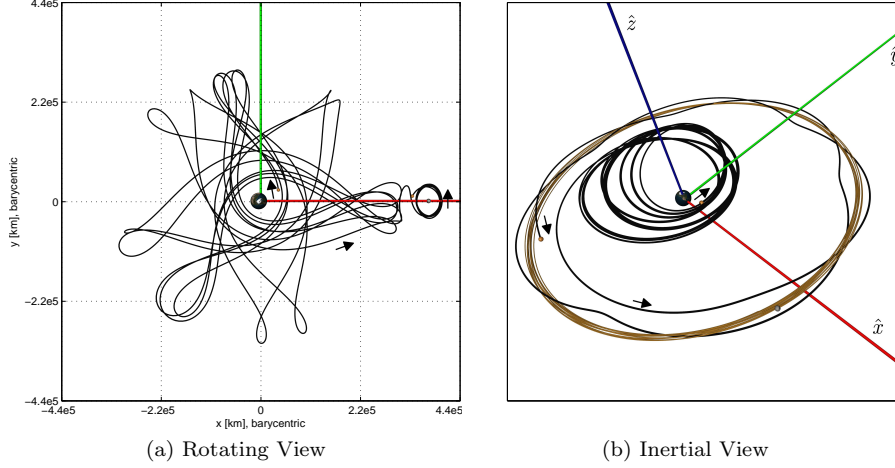

(a) Rotating View (b) Inertial View

Fig. 7: Corrected Ephemeris Solution

are numerically corrected for velocity and position continuity to within $3 \times 10^{-6} \frac{\text{m}}{\text{s}}$ and 0.8 m, respectively. The ephemeris solution necessarily experiences fully three-dimensional motion with maximum out-of-plane excursions greater than 2000 km. The convergence of the solution in the higher-fidelity model lends support to the process of seeking solutions by perturbing in position space as well as velocity space. Not only can the relatively complex solution be corrected in the simplified three-body model, but it can also be replicated in a system that mimics the actual three-dimensional behavior of the primary bodies.

5.1.2 A more general case.

Before leaving the three-body problem as the primary model for analysis, another example serves to further reinforce the extensibility and flexibility of the flow control segment approach for identifying transfer trajectories. In this case, still in the Earth–Moon CRP, the system energy level is increased as reflected by a smaller Jacobi constant value of $C = 3.05$. Given this energy value, both the gateway allowing passage into the lunar region as well as the gateway offering exit from the system are open. That is, trajectories can transit through both the L_1 and L_2 regions. Consequently, the chaoticity of the resulting map space is increased.

To illustrate the continued applicability of the control segment approach, two map points are selected arbitrarily as control points for this example. These points

are marked as "0" in Figure 8. In this case, there are no initial or terminal orbits, but rather the situation reflects the general notion of a spacecraft currently at some
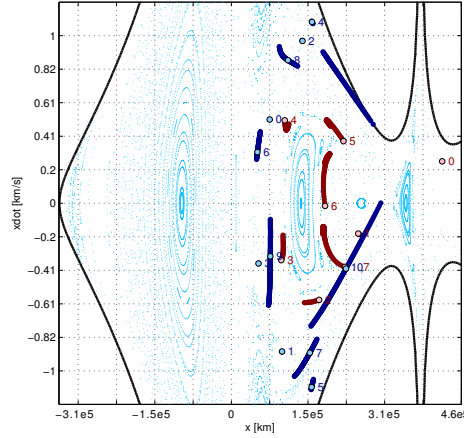

Fig. 8: Generic Control Points and Advected Curves

arbitrary state while it is desirable for it to be elsewhere in the state space. Subsequent iterations from the initial states of the associated $\boldsymbol{\xi}_2$ (1×10^{-4}) segments are also numbered in Figure 8. After 10 forward iterations (blue) and 7 backward iterations (red) a near intersection is observed. The discontinuity at the intersection point is significant, however, the end-to-end trajectory is otherwise well-behaved and the differential corrections process converges upon a solution quickly. As seen previously, this trajectory is transitioned to the higher-fidelity model. In this example, since there are no revolutions about the Moon, the ephemeris solution more closely resembles the CRP solution. The corrected CRP and ephemeris trajectories appear (both in the rotating frame) in Figure 9. In the solution computed in the restricted problem, a maneuver of magnitude 0.70 $\frac{\mathrm{m}}{\mathrm{s}}$ is required at the departure point, while a 0.76 $\frac{\mathrm{m}}{\mathrm{s}}$ maneuver is required upon arrival at the final state (total: 1.46 $\frac{\mathrm{m}}{\mathrm{s}}$ with a time-of-flight just under 372 days). This example further establishes the stretchline/FCS targeting approach and demonstrates its application in more generic situations.

5.2 System-to-system FCS example

The major focus in this investigation is illustrated by an example involving the flow control segment approach for targeting trajectories in the bicircular four-body problem. The motivating purpose behind this sample application is the possibility afforded of identifying solutions directly in a complex, nonautonomous model, a model that is not necessarily amenable to analysis methods that apply in simpler problems. The solutions that are constructed with this flow-based methodology represent trajectories that, inherently and simultaneously, accommodate, and thereby exploit, all gravitational forces available in the system. Leveraging all available natural forces frequently leads to various fuel-efficient solutions, but

(a) Corrected CRP Solution   (b) Corrected Ephemeris Solution
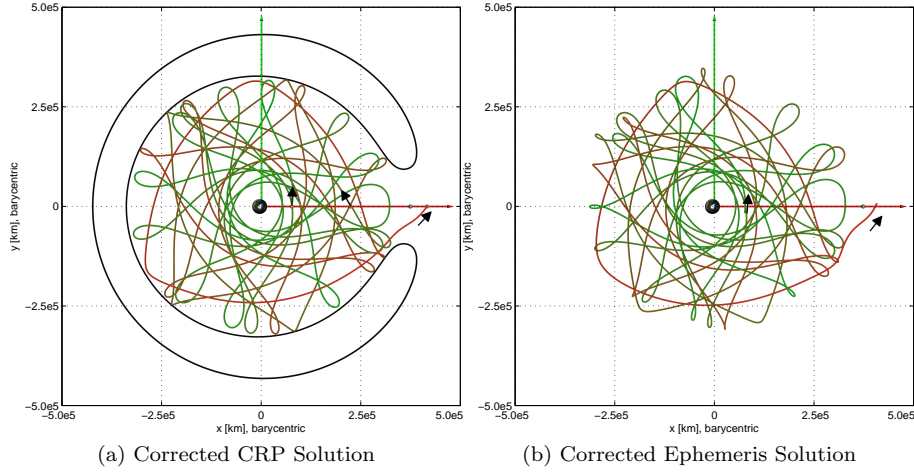
Fig. 9: Connection of Arbitrarily Selected Map Points

may result in longer times of flight. However, without flow-based tools, other, less-direct strategies must be utilized to determine solutions, and the associated solution space is generally more restricted and potentially less transparent.

The bicircular four-body model is selected to provide a convenient context for a system-to-system transfer and to explore its increased complexity as a nonautonomous system. While the selected model is time-periodic and could be made autonomous with a stroboscopic mapping, the goal is to highlight the applicability of the present methodology to nonautonomous systems. The Uranus–Titania–Oberon system is selected for its mass and distance characteristics. Titania and Oberon are the same order of magnitude in mass, possessing two-body gravitational parameters of $Gm = 228.2 \ \frac{\mathrm{km}^3}{\mathrm{s}^2}$ and $Gm = 192.4 \ \frac{\mathrm{km}^3}{\mathrm{s}^2}$, respectively, while the mass parameter of Uranus is equal to 5,793,939 $\frac{\mathrm{km}^3}{\mathrm{s}^2}$ (Jacobson (2007)). Moreover, the moons' orbits are relatively close to Uranus as well as each other with semimajor axes of ∼4.36×10^5 and ∼5.83×10^5 kilometers with respect to Uranus. Finally, the orbits of both Titania and Oberon about Uranus are relatively circular (eccentricities: 0.0011 and 0.0014, respectively) and have low inclinations with respect to the Uranian equator (0.079º and 0.068º, respectively) (Laskar and Jacobson 1987). Together, these considerations supply significant perturbing influences from the third primary, i.e., Oberon, to the behavior from the perspective of the Uranus–Titania (UT) system (as well as significant perturbations from Titania on motion as observed in the Uranus–Oberon (UO) system). Koon et al. (2002) introduces a similar system-to-system analysis using manifolds in the patched circular restricted problems involving Jupiter–Europa and Jupiter–Ganymede. Kakoi et al. (2014) also invokes similar methodology in mixed three-body systems to achieve transfers between orbits in various systems.

For an illustration of the present concept, both Uranian satellites are depicted in Figure 10 in the Uranus–Titania rotating frame, along with artificial (in this model and frame) zero-velocity curves for energy levels that supply the necessary gateway dynamics *in the CRP*. Oberon's circular orbital path also appears in gold.

The objective in the example is a trajectory that experiences a revolution about
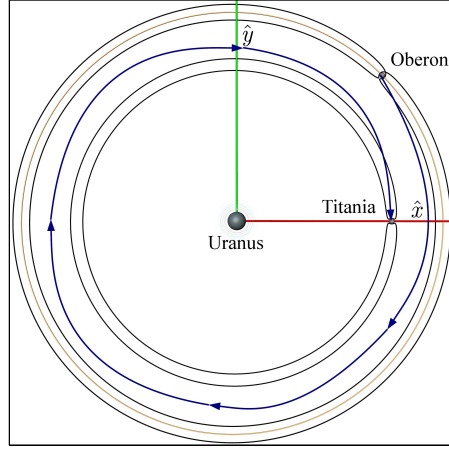

Fig. 10: System-to-System Transfer Illustration in Uranus–Titania (UT) Rotating Frame; Inspired by Figure 1.1 of Koon et al. (2002)

Oberon and then departs toward Titania, ultimately concluding with a revolution of Titania after following a transfer similar to the blue "path" sketched in Figure 10. Despite the inclusion of three-body zero-velocity curves for illustration in Figure 10, there are no convenient bounds on energy like those available in the restricted problem. Taken in turn, both Titania and Oberon are incorporated as the "additional" body, thus, the third massive primary may circumscribe (or be circumscribed by) the second. In Figure 10, Oberon is placed at an initial angle of $\frac{\pi}{4}$ radians with respect to x axis in the rotating Uranus–Titania frame (or, viewed alternately, Titania is depicted at $-\frac{\pi}{4}$ radians in the Uranus–Oberon rotating frame). For consistency, trajectory segments departing the Oberon region and moving inward toward Titania and Uranus are phased such that Oberon initiates in the geometry depicted in Figure 10. Trajectories that depart the Titania region outward toward Oberon (i.e., in reverse time) reflect the effects of Oberon originating elsewhere than at $\frac{\pi}{4}$ radians, barring coincidence.

The process blends together each of the flow-based concepts previously detailed to identify transfer solutions. Maps of FTLE values enhanced with reduced strainlines aid in the selection of candidate initial states while 4D stretchlines are employed as flow control segments to identify intersecting trajectories. The general transfer mechanism is described as follows:

1. Choose two-dimensional sections Σ_1 and Σ_2 near Oberon and Titania, and compute the respective backward and forward FTLE maps and strainlines.
2. Use the previous result to determine two orbits, one going toward Titania in forward time and the other directed to Oberon in backward time.
3. From the initial conditions in the previous step, compute the $\boldsymbol{\xi}_4$ vectors for forward and backward integration times and iterate the $\boldsymbol{\xi}_4$ stretchlines (FCS) from positions consistent with their respective sections (Σ_1 and Σ_2) to an

intermediate section Σ_3. In this step, the integration time for evaluating the Cauchy–Green tensor and obtaining $\boldsymbol{\xi}_4$ is selected consistent with the time required for the initial conditions to evolve to the intermediate section in the respective time directions.

A detailed description of the implementation of the above steps to obtain a transfer from Oberon to Titania follows. To isolate the desired behavior near Oberon and Titania, surfaces of section (generically, Σ) are constructed in the y–$\dot{y}$ phase space just beyond the gateways near L_1 and L_2, as illustrated in Figure 11. The sections are defined consistent with $-0.035 \leq y \leq 0.035$ nondimensional units (nd) and $-0.03 \leq \dot{y} \leq 0.03$ nd. These ranges translate to $-1.55 \times 10^4 \lesssim y \lesssim 1.55 \times$
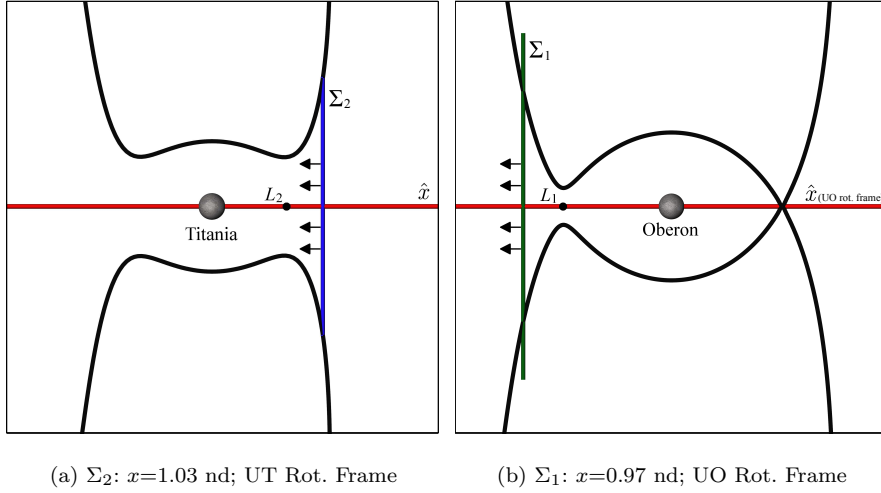

(a) Σ_2: x=1.03 nd; UT Rot. Frame   (b) Σ_1: x=0.97 nd; UO Rot. Frame

Fig. 11: Surfaces of Section for FTLE Grids

10^4 km and $-0.1094 \lesssim \dot{y} \lesssim 0.1094 \frac{\text{km}}{\text{s}}$ with $\Sigma_2 : x \approx 4.49 \times 10^5$ km (1.03 nd) in the Uranus–Titania system. In the Uranus–Oberon system, the section definition dimensionalizes to $-2.05 \times 10^4 \lesssim y \lesssim 2.05 \times 10^4$ km and $-0.0945 \lesssim \dot{y} \lesssim 0.0945 \frac{\text{km}}{\text{s}}$ with $\Sigma_1 : x \approx 5.66 \times 10^5$ km (0.97 nd). In both cases, $\dot{x}$ is recovered from the CRP Jacobi constant value consistent with the ZVC depicted in Figures 10 & 11 (in fact, each value of C equals 3.004316 in its respective system). Specifically, the negative root is selected in the evaluation of $\dot{x}$ for both maps. Consequently, $\dot{x}$ is directed (for forward time evolution) "inward" toward Uranus as indicated by arrows in Figure 11. As demonstrated by Short and Howell (2014), the associated initial conditions (IC) can be transitioned and evolved in another model—in this case, the IC are advected in the four-body model. Values of FTLE, resulting from forward integration for 10 nondimensional time steps (~13.8 days) into the Titania region as well as backward evolution toward Oberon (10 nd; ~21.4 days), appear colored consistent with the color scales in Figure 12(a,b). The two states investigated in this example are marked with black dots in Figure 12(a–d). When these states are evolved away from their respective sections in the opposite time direction, they

are integrated for longer time durations, namely, the time required to cross the intermediate hyperplane. An area of particular numerical sensitivity is apparent in Figure 12(a,c) as a solid white curve of FTLE values interior to the main lobe. This white region, as well as the areas beyond the larger gray shape on both maps, reflect FTLE values set to zero based on integration issues or exclusion by the CRP zero-velocity bounds.

Reduced strainlines are projected onto the FTLE maps in Figure 12(c,d). These strainlines help to characterize the flow originating from initial conditions and highlight various regions in the map. In fact, the reduced strainlines are cross sections of the strongest repelling hypersurfaces in the flow, and, as such, they are expected to separate regions of different behavior. The calculation of reduced strainlines results in 4D parameterizations of Lagrangian coherent structure cross sections. Not only do the strainlines offer an immediate visual indication of different flow regions, useful in searching for potential trajectory options, but they can also be directly harnessed in algorithms with precise calculated states. Given the

(a) Titania L_2 FTLE Gateway Map   (b) Oberon L_1 FTLE Gateway Map

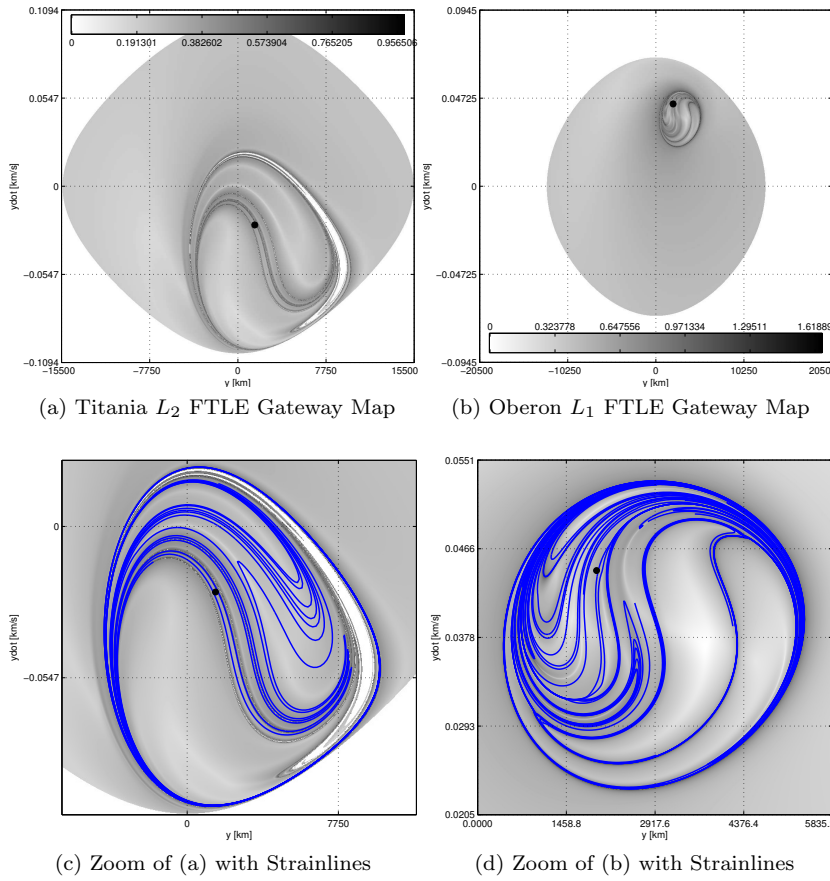(c) Zoom of (a) with Strainlines   (d) Zoom of (b) with Strainlines

Fig. 12: Maps of FTLE Values Near Titania and Oberon and Reduced Strainlines

sensitive, chaotic nature of models for simulating astrodynamical systems, very small inaccuracies (even on the order of double precision numerical truncation errors) can be significant. Extracting an accurate solution for LCS states through reduced strainlines enables additional numerical analysis within a region. The process for producing the reduced strainlines is enumerated and elaborated:

1. Identify LCS candidate points based on high FTLE values, and refine these points by seeking nearby maxima.
2. Calculate the Cauchy–Green tensor associated with the refined points and extract the CG eigenvectors.
3. Using the eigenvector directions and two normals $\boldsymbol{n}_1$ and $\boldsymbol{n}_2$ to the state space, calculate the unique direction orthogonal to $\boldsymbol{n}_1, \boldsymbol{n}_2$ and $\boldsymbol{\xi}_4$, which is the tangent direction for reduced strainlines.

In general, if the state space is defined by scalar functions $F_i = c_i$, then ∇F_i are vectors orthogonal to the state space. In the following calculations, the state space is defined by fixing an initial Jacobi constant value, $C(x, y, \dot{x}, \dot{y}) = C_\mathrm{o}$, and $x = x_\mathrm{o}$ and the vectors $\boldsymbol{n}_1 = \nabla C$ and $\boldsymbol{n}_2 = (1, 0, 0, 0)$ are used as the normals to the state space necessary to compute the reduced strainlines. The strainlines, then, follow the resulting vectors under numerical propagation and outline distinct regions characteristic of specific flow behavior. The parameterized strainlines can be exploited to evolve the associated LCS, which supplies flow pathways through the system. The curves also allow for a precise definition of region boundaries making it possible to perform additional analysis within a region. The process for constructing these strainlines is elaborated.

Identify and refine points. The initial effort of seeding points for strainlines requires some care. Manually placing initial points for strainlines guided by the features in an FTLE map may be a useful strategy. However, a more automated possibility is available. Begin with a simple line search across the FTLE field identifying all local maxima along this line. In fact, the process for identifying the initial points for the strainlines in Figure 12(c,d) is initiated from four such line searches: a horizontal line centered vertically and running across the field, a vertical line centered horizontally and running from the top to the bottom of the field, and two diagonal lines joining opposing corners. This search strategy is depicted in Figure 13(a) where darker colors represent higher FTLE values—black lines represent the search space and white dots illustrate potential maxima of the underlying FTLE field. The FTLE profile along a particular line is noisy in some regions leading to multiple local maxima in a small neighborhood and may benefit from subsampling or culling. It is desirable to identify local FTLE maxima along a line to sufficient numerical precision that the resulting CG eigenvectors are consistent and usable. Given the several maximal points identified along a field-wide line, a refinement to isolate a constrained maximum in their local neighborhoods is performed. This refinement is illustrated in Figure 13(b) centered on a single white point from one of the initial lines. Additional searches along much smaller lines (in this case $\sim 2 \times 10^{-4}$ nd, or about $300\times$ smaller than the larger lines) in the local neighborhood supply the maximum line-wise FTLE values (gray points in the figure), from among which the overall maximum is selected (black marker) as the refined point for further analysis. To accomplish arbitrary resolution (and overcome truncation errors from finite-differencing) along any of the line searches,

(a) Search Strategy for High FTLE Points: White markers represent local maxima from line searches (indicated by black "spokes").

(b) Local Maxima Refinement: Central point (white) from (a) on $\sim 300\times$ smaller spokes, overall maximum in black.
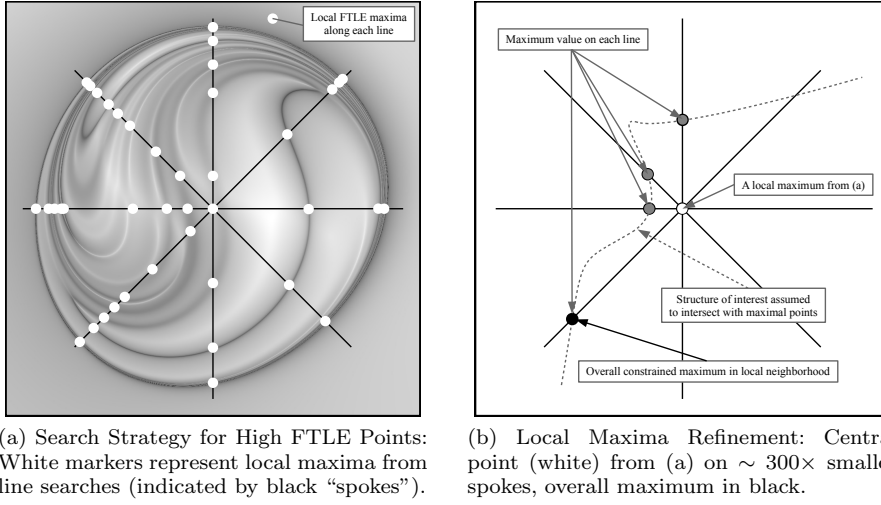
Fig. 13: Identifying and Refining LCS Candidate Points from Local FTLE Maxima

complex-step differentiation as described by Squire and Trapp (1998) is invoked to evaluate the CGST. None of the line-wise refined points is necessarily the global maximum in the neighborhood, but they are assumed to be crossings of a curve of interest (also depicted in Figure 13(b)).

Calculate Cauchy–Green eigenvectors. The Cauchy–Green tensor is evaluated for the points identified in the preceding step. The flow parameters are consistent with the parameters defining the FTLE maps. Hence, the integration time associated with the map is employed to calculate the CGST at each step. The CG eigenvectors from the associated points are retained for the subsequent step.

Identify vectors and calculate strainlines. The FTLE maps in Figure 12 involve guiding considerations. Namely, insight from the three-body Jacobi constant and the related motion boundaries are employed to fully determine the map initial conditions and selection of forward-time velocity directions consistent with Figure 11 are both invoked to produce the maps. These considerations translate to constraints that prove useful for deriving vectors to construct strainlines. Beginning with a seed point identified through refinement, a vector is calculated that is simultaneously orthogonal to the CG eigenvector $\boldsymbol{\xi}_4$, the hyperplane and the variation of Jacobi constant (i.e., the gradient of the Jacobi constant expression), as described previously. This *reduced* vector is tangent to the desired strainline and a single numerical integration step along the four-dimensional vector evolves the strainline forward to a new point. The calculation of a new reduced vector is accomplished by evaluating the CGST at the new point and again completing the requisite vector operations. This process continues for each integration step until some prescribed final integration time (i.e., a 4D arc length) is met.

The reduced repelling strainlines on the y–$\dot{y}$ FTLE maps are computed. In general, the reduced strainlines represent potential structures that can signify a

qualitative change in trajectory behavior. Particular regions are revealed where trajectories enter the nearby Uranian moon's neighborhood, and do not subsequently exit (for the duration of the simulation). These ideas are illustrated in Figure 14. The three-body ZVC (dark gray) are included in Figure 14 for context and the appropriate surface of section from Figures 10 and 11 is consistent with the green line. The outermost strainline in the central pane represents a flow boundary; states exterior to this boundary will not evolve into the Oberon region while states inside the contour will evolve toward Oberon. This outermost strainline is analogous to the boundaries reflected by the Jacobi limiting curves from the autonomous CRP where, in that case, the curve would correspond to the map image of a four-dimensional invariant manifold. In the nonautonomous four-body case the structures emerge solely as a reflection of the flow behavior. While trajectory behavior is generally consistent with the Jacobi limiting curves of the CRP, it does not, in fact, strictly conform to the underlying energy preservation of the restricted three-body problem (and the associated motion boundaries). In the left- and rightmost panes of Figure 14, the evolution of two states, one exterior (pane b.1) and one interior (pane b.2) to the outermost reduced strainline, is depicted. This illustrates the notion of the observed flow separation associated with this particular reduced strainline. Also depicted are two sets (panes a.1–3, and c.1–3) of three trajectories each taken from two distinct regions. Both sets display qualitatively similar behavior between their members and serve to illustrate the concept that states within specific regions, identifiable by the underlying FTLE features and the associated strainlines, display consistent characteristics while those belonging to other regions differ. Not all of the displayed reduced strainlines correspond to a drastic flow distinguishing feature like that associated with the outermost curve, however, they do represent more subtle changes in the state space. A particular strainline may signify a change in sign in a particular final state or a reversal in the evolution of trajectory behavior. For example, observing states on the map as they approach and cross strainlines may result in trajectories that display growth in terms of the final value of an orbital element, reach a stationary point, and then begin to reverse the previous growth. In general, the curves augment and enhance the map and supply a parameterized set of points to aid in additional analysis.

Given the guiding tools available from the maps, end-segment trajectory arcs can be identified. To help illustrate the FCS concept, segments are selected somewhat arbitrarily. That is, segments that evolve from the map and complete a few revolutions about the associated primary without impacting are desirable, but for the purposes of the ensuing example any, not necessarily the best, such arcs will suffice. Many possible choices are available and, from among these, the arcs consistent with the large black dots on the maps in Figure 12 are selected. In the case of the associated Oberon segment, the selection is consistent with the first ~1.5 revolutions of the trajectory depicted in pane a.1 of Figure 14. Both end-segment trajectories appear in Figure 15 colored from green to red with increasing time. These initial segments and the corresponding FTLE maps are each calculated with the associated primary acting as P_2 in the four-body system. For example, the Oberon segment and map are calculated in the Uranus–Oberon rotating frame with Titania orbiting counter-clockwise "interior" to Oberon. In this case, Titania's motion initiates at an angle of $-\frac{\pi}{4}$ radians with respect to the Uranus–Oberon rotating x axis. Similarly, for the Titania segment, Oberon orbits
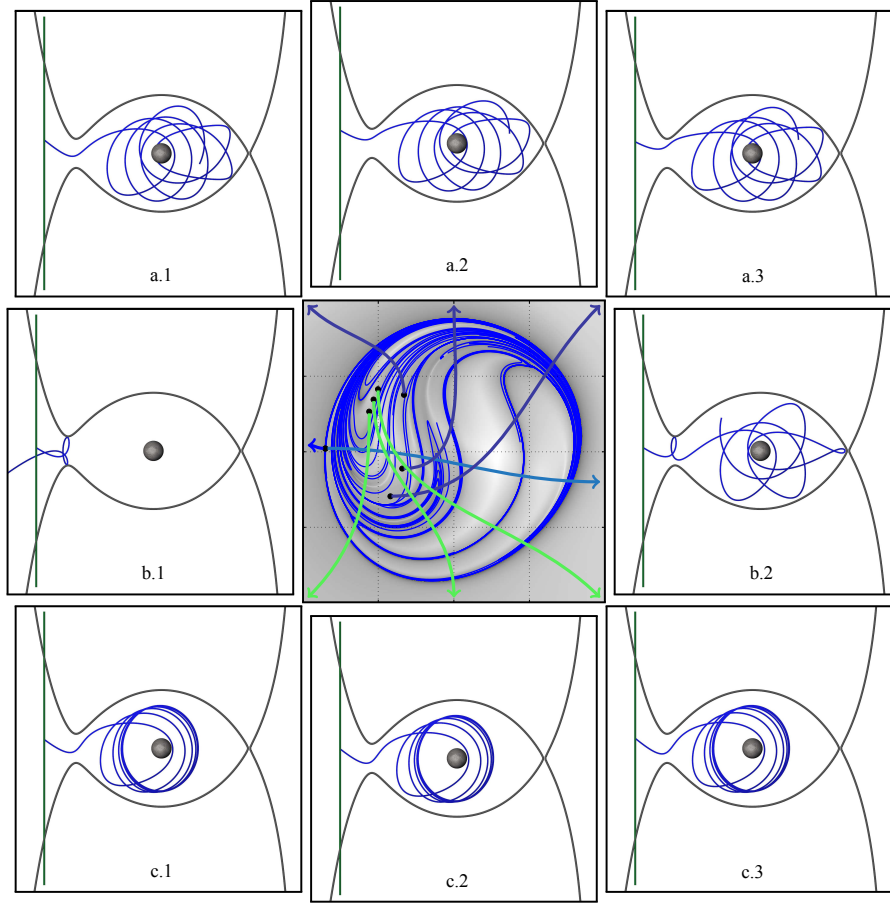
Fig. 14: Selected Trajectories (10 nd) from a Strainline Enhanced FTLE Map

the system "exterior" to Titania. However, Oberon orbits in a clockwise direction given a slower angular rate than Titania.

To simplify the analysis, the initial Oberon map state is transformed into the Uranus–Titania rotating frame using transformation matrices similar to those in Anderson (2005) and, subsequently, evolved backward in time to verify its consistency under the alternate system. All additional analysis occurs in the Uranus–Titania rotating frame. Next, the states from the two map points are evolved, forward in time from the vicinity of Oberon and backward in time from the vicinity of Titania. These propagations are terminated after successive intersections with the negative x-axis segment colored magenta in Figure 16. This selection of the intersection region is inspired by Koon et al. (2002). The forward propagation from the vicinity of Oberon always originates with Oberon at $\frac{\pi}{4}$ rad in the Uranus–Titania rotating frame. The first crossings of the forward and backward propagations are displayed in Figure 16(a), and subsequent crossings in both forward and backward time are displayed, for illustration, in Figure 16(b). The backward propagation of
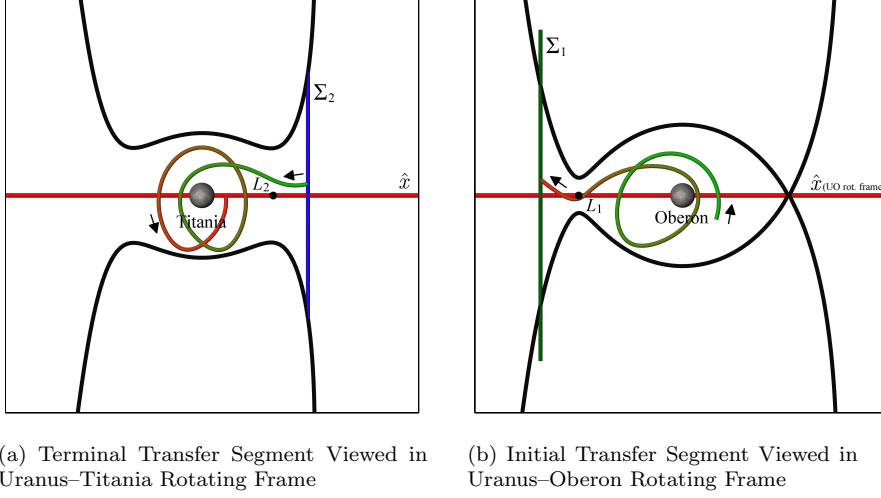
(a) Terminal Transfer Segment Viewed in
Uranus–Titania Rotating Frame

(b) Initial Transfer Segment Viewed in
Uranus–Oberon Rotating Frame

Fig. 15: Transfer "Bookends": Originating Near Oberon, Terminating Near Titania
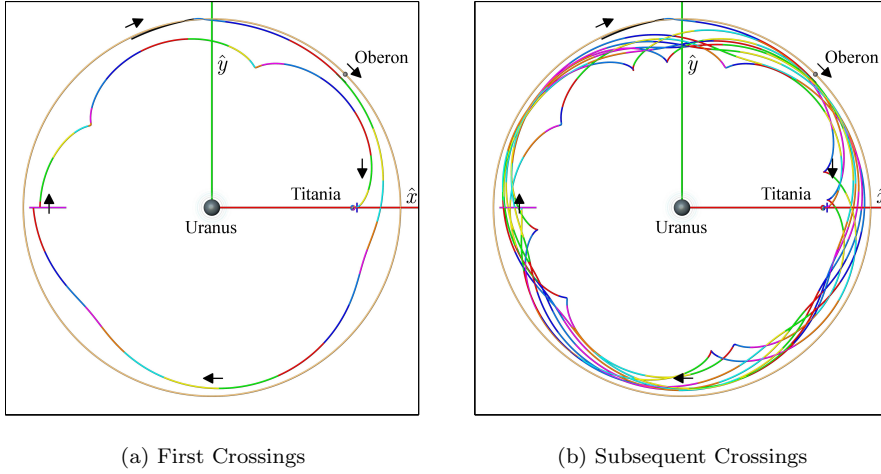

(a) First Crossings

(b) Subsequent Crossings

Fig. 16: Negative x-axis Trajectory Crossings

the Oberon trajectory (from Figure 15(b)) in the Uranus–Titania–Oberon four-body system appears at the top in both Figures 16(a,b), initially colored black and evolving toward Oberon. Oberon's circular path is represented in gold, while the spacecraft trajectory segments are colored using a discrete, rotating color scheme that increments with each full nondimensional time unit (∼1.38 days) as a means to aid in the time correlation. Forward and backward segments colored differently upon intersection immediately reveal a timing mismatch.

For the backward propagation from Titania to be valid, the initial angular position of Oberon must be adjusted. This adjustment is accomplished by summing

the time required for the forward propagation from Oberon to the nth crossing with the length of time required for the backward propagations to meet the x axis after m crossings. Given the total "inner" time duration (the forward time from the Oberon section plus the backward time from the Titania section), the angular position of Oberon is adjusted using its *constant* angular rate. However, the adjusted initial position impacts the time for the backward propagations to reach the x axis, so this adjustment procedure must be iterated until the timing and the initial Oberon position agree. In some cases, close primary passages cause this iterative process to diverge. Consequently, some combinations of forward and backward crossings are not attainable. Finally, it must be verified that the Titania end-segment (and, indirectly, the associated FTLE map) remains valid for the adjusted Oberon positions. The proximity to Titania generally overwhelms the perturbation from Oberon—its effects are still visible but, for each of the sampled cases, the selected trajectory near Titania remains qualitatively consistent. Given corrected timing and angular positions for Oberon, the Cauchy–Green tensor and its eigenvalue/eigenvector sets can be computed.

The present analysis is restricted to perturbations in velocity space along the associated eigenvector components and ultimately reveals solutions continuous in position that require three distinct velocity-changing maneuvers. The maximum perturbation associated with the segments is 1×10^{-2} or about $36 \frac{\text{m}}{\text{s}}$ to induce sufficient stretching, i.e., the end points of the segments represent a $36 \frac{\text{m}}{\text{s}}$ change in velocity. In Figure 17, the first forward crossing of the segment is depicted in
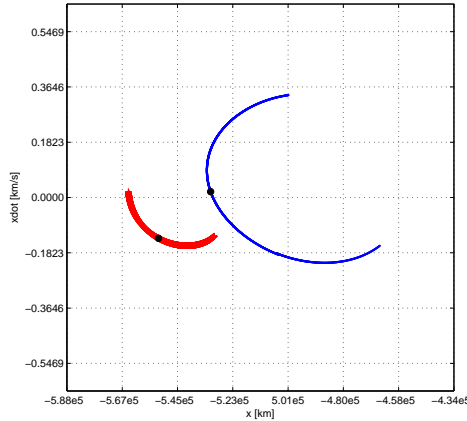

Fig. 17: Initial FCS Images on Σ_3 Hyperplane (on the Negative x Axis)

red, while the first backward crossing is colored blue. The images of the "central" trajectories about which the FCS are taken are also depicted as black dots in Figure 17. No intersections exist between the $36 \frac{\text{m}}{\text{s}}$ forward and backward FCS as is apparent in the figure. Additional revolutions are observed to supply multiple potential connections, however. A sampling of representative FCS images on the hyperplane appears as Figure 18. While the forward images will remain the same given their consistent initiating system geometry, the images of the backward FCS will vary significantly depending on the particular intersecting states and the

associated time of flight to reach the intersection. In Figure 18, the 1st-3rd forward crossings of the $\boldsymbol{\xi}_4$-velocity aligned segments from the Oberon region are marked columnwise in red, respectively from left to right. At the same time, the associated 1st-3rd backward crossings proceed by rows with the 1st crossings depicted by blue points in the first row, the 2nd crossings represented with green points on the second row, and the 3rd crossings marked by black dots in the final row. It is apparent that the resulting backward FCS images are all different contingent upon the associated forward time of flight.

Inspection of the resulting intersections in Figure 18 reveals multiple connections. However, the new "time-to-crossing" associated with the perturbed states that should ultimately lead to an intersection must be incorporated. To do so, a potential intersection is selected from map images associated with the timing that is consistent with the "central" trajectories. Then, the times of flight associated with these candidate arcs are employed to adjust the initial placement of Oberon for the backward propagation from Titania (i.e., this state, in fact, represents the final position of Oberon once the trajectory arrives in the Titania region after transferring from Oberon in forward time). The candidate intersection now occurs elsewhere along the FCS, and, in cases of intersections near the edges of the control segments or intermediate close primary passages, may no longer exist. Frequently, the intersection is still apparent on the map and the new intersecting states are subsequently employed to repeat the process, which continues iteratively until agreement in timing and system geometry occurs. One example of the transfer initiating on the Oberon section and terminating at the Titania section is displayed in Figure 19. This particular case is selected for display simply to illustrate the result of the process.

Multiple solutions are tabulated in Table 1 where the total maneuver cost associated with the Oberon section departure (i.e., the perturbation along the FCS), the adjustment in $\dot{y}$ required at the intermediate section, and the perturbation along the control segment at the Titania section is listed. The transfer time of flight is also included. Of particular note is the shortest time-duration transfer (81.56 days) characteristic of two forward and one backward iterations as well as the lowest (propellant) cost solution (123.43 $\frac{\text{m}}{\text{s}}$) from three forward and one backward crossings—these minimal cases belong to different solutions. While the main goal of this analysis is to highlight the ability of identifying solutions directly in systems incorporating higher-fidelity gravity models, some comparison with times of flight and maneuver costs associated with transfers in simpler models is useful. A Hohmann transfer between the two sections depicted in Figures 11 and 15, assuming the possibility of a 180° transfer angle, would require 5.46 days with a maneuver cost of 391.53 $\frac{\text{m}}{\text{s}}$. The orbital anomalies of Oberon and Titania at departure as well as that of Titania at arrival corresponding to the lowest propellant consumption listed in Table 1 reflects a transfer angle of 260.17^{o}. The solution in the table attends multiple revolutions of Titania and Oberon but the initial and final locations of the moons are consistent with a direct transfer experiencing less than one inertial revolution consistent with a 260.17^{o} transfer angle. A Lambert-arc solution for the given geometry is accomplished in 6.29 days and requires 458.56 $\frac{\text{m}}{\text{s}}$ to match velocities at departure and arrival. Finally, comparisons of the Jacobi constant values at the two sections computed in a common Uranus–Titania three-body system indicate a minimum CRP change in velocity of 150.99 $\frac{\text{m}}{\text{s}}$ that is necessary to supply the requisite energy change. While the solutions identified
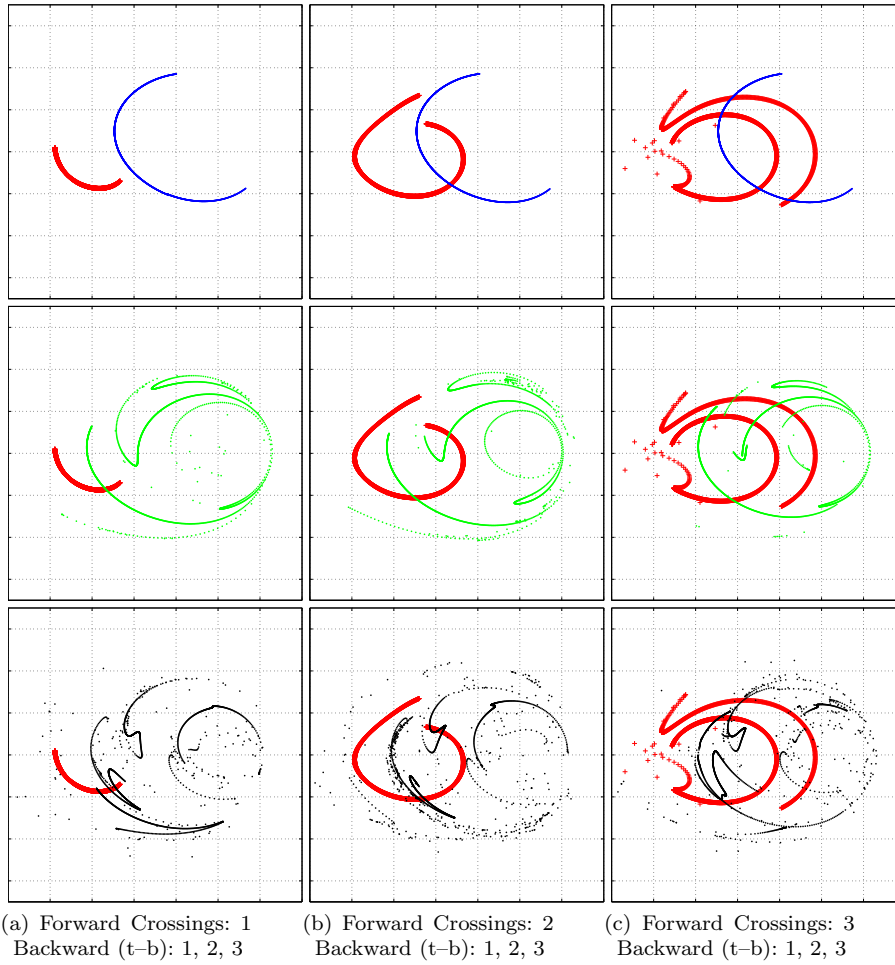
(a) Forward Crossings: 1
Backward (t–b): 1, 2, 3

(b) Forward Crossings: 2
Backward (t–b): 1, 2, 3

(c) Forward Crossings: 3
Backward (t–b): 1, 2, 3

Fig. 18: Crossing Combinations: The 1st–3rd forward crossings of the $\boldsymbol{\xi}_4$-velocity aligned segments from the Oberon region are marked in red from left to right. Representative 1st–3rd backward crossings are marked with blue, green and black points from top to bottom. The grid lines in each panel are consistent with the axis ticks in Figure 17.

from the FCS analysis involve significantly longer times of flight than simple comparisons from the two- and three-body models, they are obtained directly in the higher-fidelity model incorporating the gravities of all relevant bodies. As a consequence, they reflect lower costs as well as potential initial guess solutions for differential corrections which may further reduce propellant requirements.
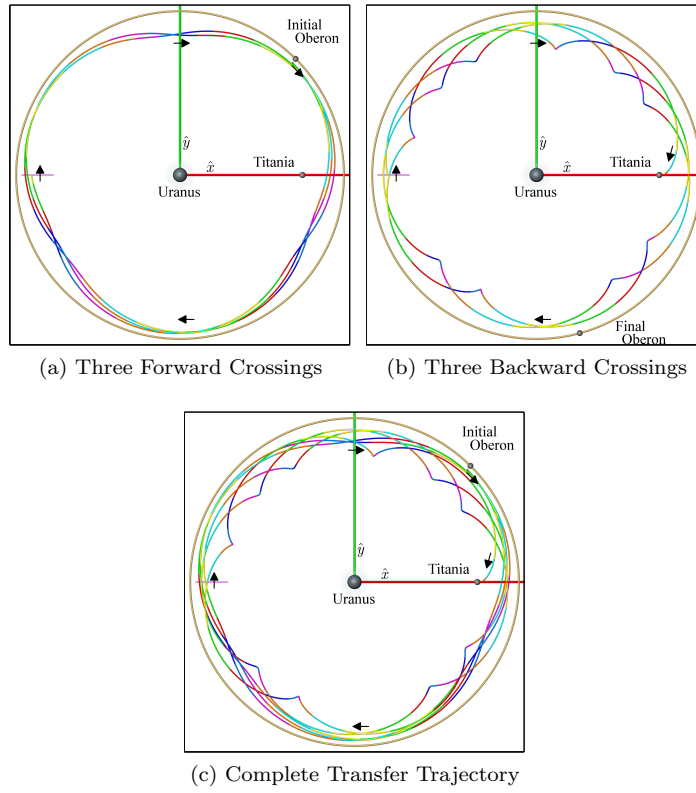
(a) Three Forward Crossings

(b) Three Backward Crossings

(c) Complete Transfer Trajectory

Fig. 19: FCS Identified System-to-system Transfer

Table 1: Transfer Data: Maneuver Costs and Times of Flight

	[m/s], [days]	[m/s], [days]	[m/s], [days]
BWD ↓ FWD →	1	2	3
1	No Intersections	182.97, 81.56	173.93, 116.41 179.46, 125.81 123.43, 119.31 163.93, 111.23
2	168.39, 91.23	142.71, 126.09 219.77, 138.94	133.74, 160.73 181.23, 186.53 167.90, 181.32 164.77, 180.81 195.42, 172.95
3	161.20, 134.90 153.86, 143.18 180.54, 142.90	126.82, 178.13 144.94, 177.99 206.28, 190.69 209.84, 190.51 208.14, 190.14	125.45, 204.55 170.13, 212.14 160.14, 247.18 182.08, 241.87 130.89, 232.53 179.08, 224.29

6 Concluding Remarks

The ability to identify flow regions that are generally advantageous to mission goals in complex astrodynamical systems expedites the search for viable options in a wide range of design scenarios. The principles of a flow-based methodology imply potential application regardless of the complexity of the underlying system, and the four-body example, in its nonautonomous form, reinforces this implication. The information supplied by the CGST augments and generalizes well-known strategies that employ the state transition matrix for trajectory design and analysis. In the case of maneuvers, knowledge of the flow behavior offers the opportunity to save propellant and time when compared to solutions that do not directly exploit the full four-body dynamics.

Since employing maneuvers in phase-space regions reflecting large stretching behavior produces larger effects downstream for smaller expense, FTLE ridges and the associated structures identify advantageous choices for maneuver placement. Specifically, control segments informed by the system flow supply excellent candidates for optimal maneuver options. Lagrangian coherent structures, their underlying theory, and the related mathematical tools characterize the flow in a system and offer valuable context.

References

Anderson, R.L.: Low Thrust Trajectory Design for Resonant Flybys and Captures Using Invariant Manifolds. Ph.D. Dissertation, University of Colorado, Boulder, Colorado (2005)

Anderson, R.L., Lo, M.W., Born, G.H.: Application of Local Lyapunov Exponents to Maneuver Design and Navigation in the Three-Body Problem. In: AAS/AIAA Astrodynamics Specialist Conference, Big Sky, Montana (2003)

Blazevski, D., Haller, G.: Hyperbolic and elliptic transport barriers in three-dimensional unsteady flows. Physica D, **273–274**, 46–64 (2014)

Blazevski, D., Ocampo, C.: Periodic orbits in the concentric circular restricted four-body problem and their invariant manifolds. Physica D, **241**, 1158–1167 (2012)

Davis, D.C., Howell, K.C.: Characterization of Trajectories Near the Smaller Primary in the Restricted Problem for Applications. Journal of Guidance, Control and Dynamics **35(1)**, 116–128 (2012)

Diacu, F.: The Solution of the n-body Problem. The Mathematical Intelligencer, **18(3)**, 66–70 (1996)

Farazmand, M., Haller, G.: Computing Lagrangian coherent structures from their variational theory. Chaos, **22**, 013128-1–12 (2012)

Froeschlé, C., Guzzo, M., and Lega, E.: The Fast Lyapunov Indicator: Detection of the Arnold web for Hamiltonian systems and symplectic mappings with 3 degrees of freedom. In: The Restless Universe, Proceedings of the 54th Scottish Universities Summer School in Physics, 327–338, Blair Atholl, Scotland (2001)

Gawlik, E.S., Marsden, J.E., du Toit, P.C., and Campagnola, S.: Lagrangian coherent structures in the planar elliptic restricted three-body problem. Celestial Mechanics and Dynamical Astronomy, **103(3)**, 227–249 (2009)

Grebow, D.: Trajectory Design in the Earth–Moon System and Lunar South Pole Coverage. Ph.D. Dissertation, Purdue University, West Lafayette, Indiana (2010)

Guzman, J.: Spacecraft Trajectory Design in the Context of a Coherent Restricted Four-Body Problem. Ph.D. Dissertation, Purdue University, West Lafayette, Indiana (2001)

Haller, G.: A variational theory of hyperbolic Lagrangian Coherent Structures. Physica D, **240**, 574–598 (2011)

Harden, G.: Automated Patch Point Placement for Autonomous Spacecraft Trajectory Targeting. M.S. Thesis, Purdue University, West Lafayette, Indiana (2013)

Harden, G.K., Haapala, A.F., Howell, K.C., Marchand, B.G.: Automated Patch Point Placement for Spacecraft Trajectory Targeting. In: AAS/AIAA Space Flight Mechanics Meeting, Santa Fe, New Mexico (2014)

Jacobson, R.A.: The Gravity Field of the Uranian System and the Orbits of the Uranian Satellites and Rings. Bulletin of the American Astronomical Society, **39**, 453 (2007)

Kakoi, M., Howell, K., Folta, D.: Access to Mars from Earth–Moon Libration Point Orbits: Manifold and Direct Options. Acta Astronautica, **102**, 269–286 (2014)

Koon, W.S., Lo, M.W., Marsden, J.E., Ross, S.D.: Constructing a Low Energy Transfer Between Jovian Moons. Contemporary Mathematics, **292**, 129–145 (2002)

Lara, M., Russell, R., Villac, B.: Classification of the Distant Stability Regions at Europa. Journal of Guidance, Control and Dynamics, **30(2)**, 409–418 (2007)

Laskar, J., Jacobson, R.A.: GUST86. An analytical ephemeris of the Uranian satellites. Astronomy and Astrophysics, **188**, 212 (1987)

Mathur, M., Haller, G., Peacock, T., Ruppert-Felsot, J., Swinney, H.: Uncovering the Lagrangian Skeleton of Turbulence. Physical Review Letters, **98**, 144502-1–4 (2007)

Oshima, K., Yanao, T.: Applications of Gravity Assists in the Bicircular and Bielliptic Restricted Four-body Problem. In: AAS/AIAA Space Flight Mechanics Meeting, Santa Fe, New Mexico (2014)

Pavlak, T.: Trajectory Design and Orbit Maintenance Strategies in Multi-Body Dynamical Regimes. Ph.D. Dissertation, Purdue University, West Lafayette, Indiana (2013)

Pavlak, T.A., Howell, K.C.: Evolution of the Out-of-Plane Amplitude for Quasi-Periodic Trajectories in the Earth–Moon System. Acta Astronautica, **81(2)**, 456–465 (2012)

Peacock, T., Dabiri, J.: Introduction to focus issue: Lagrangian coherent structures. Chaos, **20**, 017501-1–3 (2010)

Pérez, D., Gómez, G., Masdemont, J.J.: Detecting Invariant Manifolds Using Hyperbolic Lagrangian Coherent Structures. In: IAA/AAS Conference on the Dynamics and Control of Space Systems, Porto, Portugal (2012)

Schroer, C.G., Ott, E.: Targeting in Hamiltonian systems that have mixed regular/chaotic phase spaces. Chaos, **7(4)**, 512–519 (1997)

Shinbrot, T., Ott, E., Grebogi, C., Yorke, J.A.: Using chaos to direct trajectories to targets. Physical Review Letters, **65**, 3215–3218 (1990)

Short, C.R., Howell, K.C., Tricoche, X.M.: Lagrangian Coherent Structures in the Restricted Three-Body Problem. In: AAS/AIAA Space Flight Mechanics Meeting, New Orleans, Louisiana (2011)

Short, C.R., Howell, K.C.: Lagrangian coherent structures in various map representations for application to multi-body gravitational regimes. Acta Astronautica, **94(2)**, 592–607 (2014)

Smith, D.R.: An Introduction to Continuum Mechanics — after Truesdell and Noll. Kluwer, Dordrecht (1993)

Squire, W., Trapp, G.: Using Complex Variables to Estimate Derivatives of Real Functions. SIAM Review, **40(1)**, 110–112 (1998)

Szebehely, V.: Theory of Orbits, the Restricted Problem of Three Bodies. Academic Press, New York (1967)

Villac, B., Broschart, S.: Applications of Chaoticitiy Indicators to Stability Analysis Around Small Bodies. In: AAS/AIAA Space Flight Mechanics Meeting, Savannah, Georgia (2009)

Villac, B.F.: Using FLI maps for preliminary spacecraft trajectory design in multi-body environments. Celestial Mechanics and Dynamical Astronomy, **102(1–3)**, 29–48 (2008)